

# Identifying Many-Body Localization in Realistic Dot Arrays

Alexander Nico-Katz,<sup>1</sup> Gulzat Jaliel,<sup>2</sup> Paola Atkinson,<sup>3,4</sup> Thomas A. Mitchell,<sup>3</sup> David A. Ritchie,<sup>3</sup> Charles G. Smith,<sup>3</sup> and Sougato Bose<sup>1</sup>

<sup>1</sup>*Department of Physics and Astronomy, University College London, London WC1E 6BT, United Kingdom*

<sup>2</sup>*London Centre for Nanotechnology, University College London,  
17-19 Gordon Street, London WC1H 0AH, United Kingdom*

<sup>3</sup>*Cavendish Laboratory, University of Cambridge,  
J. J. Thomson Avenue, Cambridge CB3 0HE, United Kingdom*

<sup>4</sup>*Sorbonne Université, CNRS, Institut des NanoSciences de Paris, INSP, 4 place Jussieu, F-75005 Paris, France*

(Dated: January 20, 2023)

We determine whether or not it is possible to identify many-body localization in quantum dot arrays, given their current technological capacities. We analyze the phase diagram of an extended Fermi-Hubbard model - a theoretical system that quantum dot arrays are known to simulate - using several quantities of varying experimental accessibility. By deriving the parameters of our model from our experimental system, we find that many-body localization can potentially be detected in current-generation quantum dot arrays. A pitfall that we identify is that the freezing of a system due to strong interactions yields signatures similar to conventional localization. We find that the most widely-used experimental signature of localization - the imbalance - is not sensitive to this fact, and may be unsuitable as the lone identifier of the many-body localized regime.

## I. INTRODUCTION

Many-body localization (MBL), the breaking of ergodicity and corresponding arrest of transport in disordered strongly-correlated quantum systems [1–4], has become increasingly accessible in a wide array of experimental systems. Devices in which MBL has been experimentally realized include ultracold atoms and ions in optical lattices [5–8], and superconducting qubits [9], with recent evidence suggesting that extant transmon-based quantum computers naturally tread a delicate line between localization and chaos [10]. A natural, yet hitherto unrealized, setting in which to explore MBL is that of semi-conducting quantum dot arrays (QDA). Such systems are promising simulators of fermionic systems in both 1D and 2D [11, 12], they are highly tunable and different lattice geometries can be readily fabricated: in short an ideal testbed for MBL. Despite this, modern arrays are realistically limited to few dots, readout can be noisy, and - as they are extremely sensitive to environmental electrostatic discharge - they can be damaged during fabrication, handling, or general use during the experimental process. Thus, whilst the detection of MBL in realistic current-generation quantum dot arrays is both a crucial proof-of-concept for such arrays as generic quantum testbeds, it is also fraught with difficulties. A number of questions naturally arise: can current-generation realistic arrays access MBL regimes? How can we reliably identify MBL in such arrays? And - given how fragile these systems are - what are the minimal measurements required to do so?

In this article we address the above questions by first characterizing the double-dot properties of a state-of-the-art device and extrapolating the rough parameter ranges of an extended Fermi-Hubbard model that such a device can simulate. We then analyze this model numerically, investigating a variety of quantities in both bulk and lo-

cal variants. These quantities require measurements that range from density operator tomography of half the system to simple charge sensing on two sites.

In section II we introduce and discuss the model that quantum dot arrays simulate. In section III we discuss our experimental devices, namely one-dimensional lateral arrays of electrostatically defined quantum dots, and then characterize such a device to extract rough ranges for the theoretical model parameters from experimental data. We then define several quantities in both bulk and local variants in section IV which can be used to differentiate MBL from the other phases of the model. Finally, in section V we analyze the model across the extracted parameter ranges and use the aforementioned quantities to develop a protocol for identifying MBL with minimal measurements on a realistic device.

## II. MODEL AND THEORY

The theoretical model which our experimental quantum dot array simulates is that of an extended Fermi-Hubbard model restricted to a single species of electron, described by the Hamiltonian

$$H = \tau \sum_j^{L-1} (c_j^\dagger c_{j+1} + \text{h.c.}) + V \sum_j^{L-1} n_j n_{j+1} + \sum_j^L h_j n_j \quad (1)$$

where  $n_j = c_j^\dagger c_j$  is the number operator at site  $j$ . The parameters  $\tau$  and  $V$  are the tunnelling and nearest-neighbour coulomb interaction energies respectively, and the  $h_j$  are random energies drawn uniformly from the interval  $[-h, h]$ ; with  $h$  tuning the overall disorder strength. We have assumed (i) a single species of electron and (ii) a single active energy level per site.

Prototypically, these assumptions are rarely made *a*

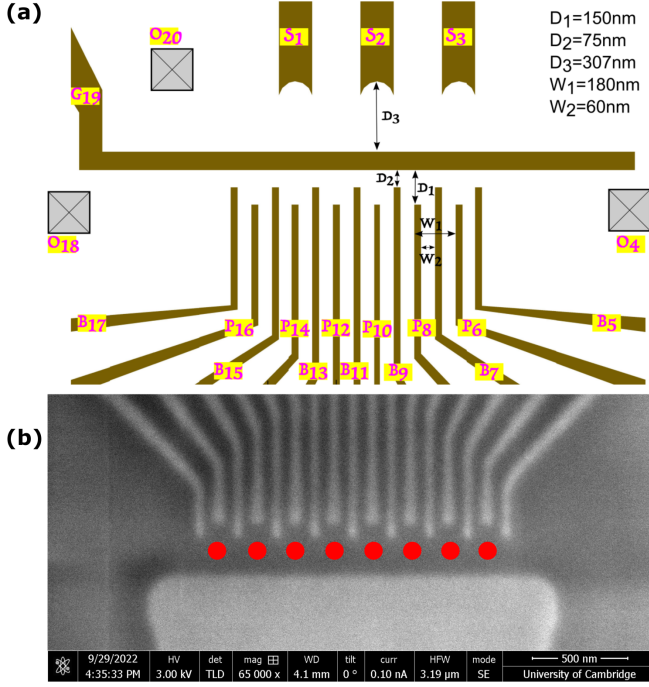


FIG. 1: (a) The six-dot design for the specific experimental device we characterize. In section III we extract rough parameter ranges for the theoretical model that the device simulates from the pair of dots defined by the gates  $G_{19} - B_{15} - B_{13} - B_{11}$  and addressed by plunger gates  $P_{14}$  and  $P_{12}$  respectively. (b) An SEM image of an array we fabricated which is similar to the design we characterize. Slight blurring of the SEM image is due to a layer of protective PMMA with an approximate thickness of 200 nm.

*priori*, and an on-site Coulomb interaction tuned by  $U$  is additionally considered. This, however, introduces an array of new tunnelling and interaction terms which dramatically confuse the process of extracting Hamiltonian parameters from experimental data; for this reason we assume that  $U$  is sufficiently large that it integrates out of our model entirely (we will later demonstrate that this assumption is well-founded in the context of our physical devices). Together, assumptions(i) and (ii) restrict us to charge number fluctuations of one electron per site: the simplest experimental setting in which we can find MBL, and the ideal setting in which to analyze the accessibility of MBL in QDA. In experiment, these two assumptions can be imposed by (i) applying a magnetic field during initialization to spin-polarize the electrons and (ii) ensuring that all energy scales  $\tau, V, h$  are kept much lower than the on-site charging energy - which is related to  $U$ .

We note here several features of the Hamiltonian of eq. (1) which are of direct relevance to our analysis. Firstly it is entirely a function of the number operators for  $\tau = 0$ , and as such is trivially diagonalizable at this point in the number basis; this corresponds to the 'classical' picture of quantum dots in the constant interaction

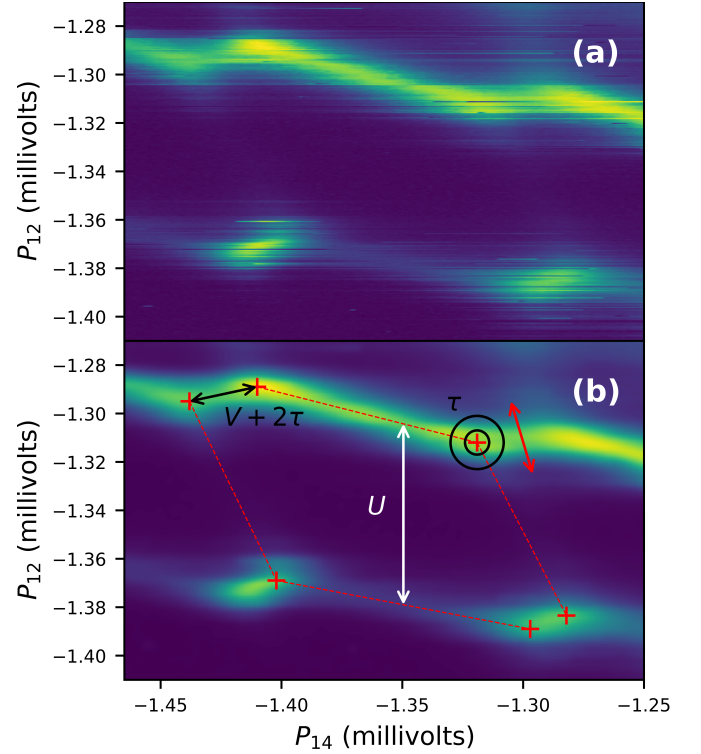


FIG. 2: (a) A typical experimental honeycomb cell of the charge-stability diagram obtained by differential conductance measurements on the two dots defined by the gates  $G_{19} - B_{15} - B_{13} - B_{11}$  in the middle of a device similar to that shown in fig. 1. Bright (dark) regions indicate higher (lower) measured values of the differential conductance as a function of the two local plunger gate voltages  $P_{14}$  and  $P_{12}$ . (b) A Gaussian smoothing of the raw data shown in panel (a) with a schematic overlay of how the parameters of the theoretical model that the device simulates are extracted from the geometry of the honeycomb cell.

model, wherein the system's ground states are classical ground states of charges on a network [13]. Secondly, the system maps directly onto an extended XXZ model (see appendix A) via the Jordan-Wigner transformation, and so inherits an insulating phase at  $V/\tau = 2$ . For  $V/\tau = 0$  the system is non-interacting and, in the thermodynamic limit, should localize for all  $h/\tau > 0$ ; this is Anderson localization - which we do not consider here. For  $0 < V/\tau < 2$  the system is conducting and interacting and so should many-body localize for sufficient  $h/\tau$ , whilst at  $V/\tau > 2$  the system is insulating. For these reasons, the ergodic-MBL transition can only be meaningfully discussed in the regime  $0 < V/\tau < 2$ , and the ability to differentiate the ergodic regime, interaction-induced insulation due to high  $V/\tau$ , and disorder-induced MBL becomes critically important when we seek to definitively identify the last in an exploratory experimental context. Finally, the systems we consider are very small in order to model the realistic scale of fully tunable experimen-

tal quantum dot arrays, as such the system is suspect to a range of pathologies. Edge effects are non-trivial, the phase transitions are expected to smear out - with e.g. Anderson localization visible for small, non-zero,  $V/\tau$  - and the nature of the MBL transition being generally suspect, potentially not reflecting behaviour in the thermodynamic limit at all.

In particular, recent research suggests that attempting to isolate the ergodic-MBL transition in such small systems is difficult - it is hard to make declarative statements about the thermodynamic transition without accessing both exponential time and length scales in microscopic analyses [14, 15], and the small-system transition may belong to a different universality class than the transition in the thermodynamic limit [16]. Rather it is better to identify different regimes and investigate their properties away from the ergodic-MBL critical line. For this reason, we do not attempt to systematically investigate criticality in this article, rather determine the conditions under which the different regimes can be *differentiated* in realistic experimental quantum dot arrays.

### III. EXPERIMENTAL SYSTEM AND ACCESSIBLE PARAMETER RANGES

The experimental devices we consider are lateral arrays of electrostatically defined quantum dots formed by selectively depleting electrons using nano-fabricated gate electrodes on the surface of a GaAs/AlGaAs heterostructure. The specific device we use as a benchmark has a gate pattern which defines a linear array of six quantum dots, the design of which is shown in fig. 1(a). A scanning electron microscope (SEM) image of a similar (eight-dot) device we fabricated is shown in fig. 1(b), where the positions of the quantum dots are illustrated by red circles. These are both simply larger versions of the designs often used in multi-dot experiments (see e.g. Refs. [11, 17]).

Tunnelling rates between adjacent dots are controlled through the voltages applied to the barrier gates  $B_j$  between neighbouring dots, where  $j$  is the gate number. On-site chemical potentials are controlled by voltages applied to the plunger gates  $P_j$ . The leftmost and the rightmost dots are also tunnel-coupled to the left and right reservoirs, respectively. The long middle bar gate, labelled  $G_{19}$  in fig. 1(a), is the top barrier for all wire gates below; and the three sensing gates, labelled  $S_{1(2)(3)}$  in fig. 1(a), are quantum point contact charge detectors. The non-linear conductance characteristics of these detector gates can be used as a sensitive probe of the local electrostatic environment [18], which in turn can be used to measure local charge fluctuations. In practice, individual gate voltages affect not only the parameters they are designed to control but, through capacitive cross-talk, also affect other electrochemical potentials and tunnel barriers. However, this effect can be compensated for by using virtual gates: linear combinations of multiple gate voltages chosen such that only a single electrochemical

potential or tunnel barrier is addressed [11, 19].

The design of the specific six-dot device used to extract our model parameters is shown in fig. 1(a). The fabrication of this device uses a Si-doped GaAs/Al<sub>x</sub>Ga<sub>1-x</sub>As heterostructure, with a two-dimensional electron gas 90nm below the surface, a mobility of  $9 \times 10^5 \text{ cm}^2/\text{Vs}$ , and an electron concentration of  $1.62 \times 10^{11} \text{ cm}^{-2}$ . All gates are fabricated in a layer of Ti/Au of thickness 5/20nm, evaporated on the bare substrate. The device was cooled in a dilution refrigerator with a base temperature of  $T \sim 70 \text{ mK}$ . The electron temperature, however, is estimated to remain at  $\sim 100 \text{ mK}$ . Extracting from their individual Coulomb diamonds, the on-site charging energy  $E_C$  is estimated to be  $\sim 1.3 \text{ meV}$ , and the zero-dimensional level spacing of an individual dot to be  $\sim 400 \mu\text{eV}$ .

We do not characterize charge-qubit coherence times, but take them to be approximately 1 – 10ns, which is in conservatively line with other characterizations in similar systems [20, 21]. Though we note that silicon-based devices and spin-qubits have coherence times orders of magnitude greater [22–25], and may be a lucrative setting in which to investigate MBL as well.

We characterize the two dots in the middle of our array, defined by the gates  $G_{19} - B_{15} - B_{13} - B_{11}$ , by scanning the applied plunger gate voltages  $P_{12}$  and  $P_{14}$  and measuring the differential conductance across the double-dot system. This yields a charge-stability diagram comprised of ‘honeycomb’ cells wherein the boundaries between stable electronic configurations admit the flow of current and appear as bright regions (high differential conductance). A typical honeycomb cell we obtained from this analysis is shown in fig. 2(a). From this cell we can determine the properties of the extended Fermi-Hubbard model that these two dots simulate (for a detailed discussion, see Ref. [13] and the thesis of T. Hensgens in Ref. [26]).

We now turn our attention to the extraction of the parameter ranges (for  $U/\tau$  and  $V/\tau$ ) of our theoretical model eq. (1) from the experimental data shown in fig. 2(a). This informs the model regimes that the experimental device can access. To facilitate this process we first process the data using a Gaussian kernel-density estimate, producing the smoothed honeycomb cell shown in fig. 2(b).

The energy  $U$  is the simplest parameter to extract, it is simply the cost of adding a new electron to the dot, including both charging and zero-dimensional energies [13]. This is simply the vertical distance between two classical ground state electron configurations, i.e. the potential we need to overcome to add a single electron to a single site [11]. In fig. 2, we have selected a honeycomb cell without a contribution from the zero-dimensional level spacing; thus this article works with a ‘worst case’ scenario where  $U/\tau$  is not strengthened by zero-dimensional effects. Even in this regime, we later find  $U/\tau$  sufficiently large to justify our assumption (ii) in section II.

The nearest-neighbour Coulomb repulsion  $V$  is related

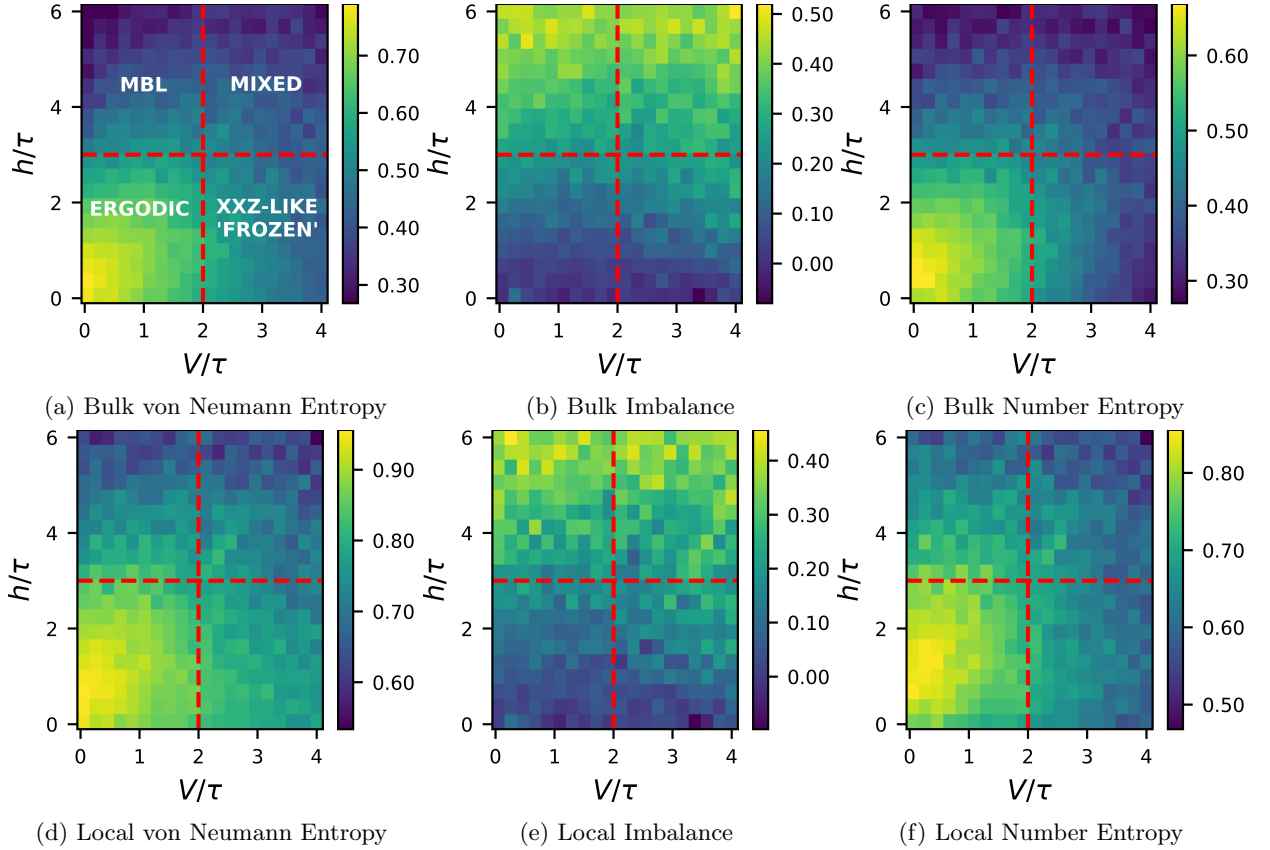


FIG. 3: Disorder-averaged late-time quantities across the full  $V - h$  phase diagram for the realistic system; initialized in a charge-density wave configuration. The realistic system consists of  $L = 8$  sites, total evolution times of  $\tau t_f = 150$ , no time-averaging (the final value at  $t_f$  is simply read out), and disorder-averaging over only 50 samples per  $(V, h)$  coordinate.

to the shortest distance between two phases which differ by a single additional electron on *both* sites, i.e. the energy required to add two electrons to neighbouring sites after overcoming the necessary on-site energy requirements. Due to hybridization caused by  $\tau$ , this distance is proportional to  $V + 2\tau$  [26].

The tunnelling energy  $\tau$  affects the classical charge stability diagram mainly through the hybridization of neighbouring classical ground states of identical total electron number; this broadens the distance between triple points and phase boundaries, and causes rounding of the phase boundaries near the classical triple points. Thus  $\tau$  can be extracted in several ways. Firstly, by analyzing the extent to which phase boundaries are curved [27]. Secondly, by extracting the tunnelling rate from Larmor oscillations observed over time as in [28, 29]. Thirdly, by numerically fitting a line cut of the charge-stability diagram along a detuning axis  $V_1 - V_2$  (the red double-headed arrow in section II) to the analytic form of the steady-state conductance through an open double-dot model, or the response of a sensing dot; both of which should broaden with increasing  $\tau$  [11–13]. As triple points are separated by a distance proportional to  $V + 2\tau$ , we estimate rough

ranges on this broadening (and thus  $\tau$ ) by estimating the maximum and minimum radii of the smeared-out triple points (shown as black rings in section II). Whilst a detailed characterization of  $\tau$  is critical in experiment, these rough estimates are sufficient to give us the range of possible  $\tau$  values across which we must understand MBL in order to determine its accessibility in QDA [30].

Altogether, approximate ranges for  $U/\tau$ , and  $V/\tau$  can be determined by the features of the charge-stability diagram. The relationships between these parameters and the geometry of a typical honeycomb cell are shown as an overlay onto the smoothed data in fig. 2(b). We manually identify suspected triple points - denoted by black crosses - and take minimum (inner) and maximum (outer) broadening radii - denoted by the inner and outer black circles respectively. The phase boundaries are derived from lines connecting these triple points, and the range of the radii yields ranges of values for  $\tau$ ,  $V + 2\tau$ , and  $U$  as annotated, and as discussed above. Our resulting estimated ranges are summarized in table I. In each case, the on-site Coulomb interaction  $U$  is found to be much larger than both  $\tau$  and  $V$ , justifying our assumption that the corresponding model has one active energy level per site.



These estimated ranges encompass extant characterizations of multi-dot arrays in e.g. Ref. [11]. Finally, we note that the  $h/\tau$  is freely tunable by altering the on-site chemical potentials by changing plunger gate voltages, and is thus only limited by the restriction that  $U \gg h$ .

Parameters	Minimum $\tau$	Maximum $\tau$
$V/\tau$	3.727	0.603
$U/\tau$	12.941	4.792

TABLE I: Table of upper and lower bounds on the considered parameter ranges for eq. (1) extrapolated from the features of the experimental charge stability diagram of fig. 2.

#### IV. PROBING QUANTITIES

We consider three quantities: the von Neumann entropy  $S$ , the widely-used imbalance  $\mathcal{I}$ , and the number entropy  $S_N$ , which vary first in their experimental accessibility and secondly - as we show in section V - their ability in differentiating regimes in the phase diagram of eq. (1).

The first quantity of interest is the von Neumann entropy which - in a bipartite pure state - unambiguously quantifies the entanglement across the bi-partition. It has been used extensively in the context of MBL theory and experiment, and serves here as a benchmark for the other quantities [31–35]. For a given subsystem  $\rho(t)$  of size  $L_\rho$  it is defined as

$$S(\rho(t)) = -\frac{1}{L_\rho} \text{Tr} [\rho(t) \log_2 \rho(t)] \quad (2)$$

where we have chosen a logarithm base 2 such that the resulting quantity is measured in bits, and that it saturates (for a single species of fermion with local dimension 2, and given that  $L_\rho/L \leq 1/2$ ) to unity. In experiment, the calculation of eq. (2) would require full tomography of the density operator of the region of interest - a prohibitively expensive and difficult task - but it serves as crucial benchmarks nonetheless.

The second quantity we consider is the imbalance, widely used in MBL [5, 36–39]. The imbalance is used to determine how much a system has deviated from an initial charge configuration, it is directly related to standard auto-correlation functions. We define it as

$$\mathcal{I}(\rho(t)) = \frac{2}{L_\rho} \sum_j \text{Tr} [\rho(0)n_j] \text{Tr} [\rho(t)n_j] \quad (3)$$

where  $j$  runs over the physical sites of the subsystem  $\rho(t)$  and where - in the case of an initial charge density wave state such that  $n_j$  has  $\rho(0)$  as an eigenstate - it reduces to the conventional statement of the imbalance as the

difference between occupancy numbers on odd and even sites. If the charge configuration of  $|\psi(t)\rangle$  becomes uncorrelated to the initial configuration of  $|\psi(0)\rangle$  then the imbalance saturates to zero  $\mathcal{I}(t) = 0$ , whereas if they remain (anti-)correlated it persists as a finite non-zero value  $\mathcal{I}(t) > 0$  ( $\mathcal{I}(t) < 0$ ). In experiment  $\mathcal{I}(\rho(t))$  requires only charge sensing on the relevant sites, which is significantly easier than the state tomography required by the von Neumann entropy.

Finally we consider the number entropy, a quantity which has seen some use in MBL [34, 40, 41], and which is simply the entropy of the discrete probability distribution  $p(\rho(t), n)$  of finding  $n$  particles in the subsystem  $\rho(t)$ , defined as

$$S_N(t) = -\frac{1}{L_\rho} \sum_N p(\rho(t), n = N) \log_2 p(\rho(t), n = N). \quad (4)$$

This quantity is directly related to the von Neumann entropy by  $S = S_N + S_C$  where  $S_C$  is the configurational entropy: the contribution to the entanglement due to configurational correlations. We can compute the distributions from the density operator by constructing projectors  $P_N = \sum_r |N_r\rangle \langle N_r|$  where  $|N_r\rangle$  are the  $N$ -particle states in the number basis that span the reduced Hilbert space of  $\rho(t)$ . The probability is then given by  $p(\rho(t), n = N) = \text{Tr}[\rho(t)P_N]$ . We calculate an ergodic limit of the number entropy in appendix D, which we use to benchmark our numerical results.

We consider both bulk and local variants of the quantities by considering three different subsystems, the full system  $\rho_f(t) = |\psi(t)\rangle \langle \psi(t)|$ , half of the system  $\rho_{hc}(t)$ , and two sites in the middle of the system  $\rho_2(t)$ . The quantities are computed using the equations in section IV using the bulk or local reduced density operators according to Table II.

Quantity	Bulk	Local
VN Entropy	$S^{(b)}(t) = S(\rho_{hc}(t))$	$S^{(l)} = S(\rho_2(t))$
Imbalance	$\mathcal{I}^{(b)}(t) = \mathcal{I}(\rho_f(t))$	$\mathcal{I}^{(l)}(t) = \mathcal{I}(\rho_2(t))$
Number Entropy	$S_N^{(b)}(t) = S_N(\rho_{hc}(t))$	$S_N^{(l)}(t) = S_N(\rho_2(t))$

TABLE II: Summary of bulk and local variants of the quantities discussed in section IV. Bulk quantities are calculated over the state of the full system  $\rho_f(t)$  or half the chain  $\rho_{hc}(t)$ , local quantities are calculated over two sites in the middle of the device  $\rho_2(t)$ . Experimentally, the imbalance and number entropy require identical local charge-sensing measurements only, and highly experimentally tractable.

In experiment the number entropy requires the same charge sensing measurements as the imbalance, but yields signatures similar to the von Neumann entropy. This becomes useful in section V where we find that the number entropy can identify phases that the imbalance cannot

without requiring the prohibitively difficult state tomography of the full von Neumann entropy. Moreover, the local variants of the quantities shown in the last column of table II, require measurements only on two sites; making their calculation even simpler in experiment.

## V. IDENTIFYING MANY-BODY LOCALIZATION IN REALISTIC DOT ARRAYS

Here we investigate the phase diagram of eq. (1) at time  $t_f$  after initialization in the charge density wave state wherein every other site is occupied at time  $t = 0$ . We vary  $V/\tau$  and  $h/\tau$ , and analyze the quantities (both bulk and local variants) discussed in section IV. Given the upper and lower bounds extracted in section III, we investigate the phase diagram across the intervals  $V/\tau \in [0, 4]$  and  $h/\tau \in [0, 6]$ . In the main text, we restrict ourselves to realistic simulations of the system, namely: system sizes of  $L = 8$  sites, intermediate time scales of  $\tau t_f/h = 150$  which (for reasonable tunnelling energies  $\tau \sim 50 - 100 \mu\text{eV}$ ) are within typical charge-qubit coherence times for these systems ( $t_f \sim 1 - 10\text{ns}$ ) [20, 21], no time-averaging - we simply read out the value at the final time  $t_f$  - and the number of disorder samples limited to 50 realizations. Additionally, we introduce large absolute  $\pm 0.1$  and relative  $\pm 5\%$  uncertainties (box-distributed) in the parameters  $h/\tau$  and  $V/\tau$  such that the couplings are non-isotropic and random for each disorder realization. This accounts for small changes in these couplings due to cross-talk, and errors in the fabrication and characterization of the device. In the appendix (see appendix B), we additionally consider an ideal system of  $L = 10$  sites in which all the above restrictions are lifted; this serves to benchmark the realistic analysis presented here.

The results of this analysis are shown in section II, wherein panels (a), (b), and (c) show the bulk von Neumann entropy, Imbalance, and Number entropy at  $t_f$  respectively, and panels (d), (e), and (f) show the local variants. Red dashed lines indicate the expected transition at  $V/\tau = 2$  and an ergodic-MBL crossing at  $h/\tau \sim 3$ . The phase diagrams of the von Neumann entropy and number entropy are qualitatively similar, with a build-up of both entropies in the thermal regime that falls off as  $h/\tau$  or  $V/\tau$  increase. Surprisingly, the imbalance doesn't seem to register the metallic-insulator transition at  $V/\tau = 2$ , instead staying close to its thermal value of zero for all values of  $V/\tau$  for sufficiently low disorder strength  $h/\tau$ . This suggests that the imbalance alone cannot unambiguously detect the presence of the MBL regime: if a transition is seen in  $h/\tau$ , it is entirely possible that the system is *already* in an insulating regime that the imbalance is simply agnostic to. As such, differentiation between the thermal, MBL, and insulating regimes requires a different quantity. The number entropy requires the same measurements as the imbalance (i.e. charge sensing as opposed to full state tomography) but is also sensitive to the transition in  $V/\tau$ . Thus by

post-processing the results of a large number of charge measurements in two different ways, the imbalance and number entropy can both be calculated and compared, with the former sensitive only to the MBL transition, and the latter sensitive to both the MBL and insulating transition.

Perhaps the most striking feature of section II is that the qualitative features of the bulk and local phase diagrams for individual quantities are consistent. For the purpose of differentiating the thermal, MBL, and insulating regimes, local measurements on a few sites seem to suffice. In conjunction with the above discussion, this leads to a simple protocol for detecting MBL in realistic QDA: perform charge-sensing measurements on a few dots in the middle of the array, then post-process these measurements differently to construct the local imbalance and local number entropy. Repeating this protocol as we scan  $h$  from a low to a high value will show a transition in both the number entropy and imbalance if the system is MBL, and only the imbalance if the system is insulating.

We suggest that both the sensitivity of the number entropy and insensitivity of the imbalance to the transition in  $V/\tau$  can be explained by a type of 'rolling' behaviour, in which the charge-density wave moves coherently through the system. In essence,  $V/\tau$  is so strong that excitations cannot exist in neighbouring sites (similar to Rydberg-blockaded systems [42–44]) and due to the fact that total particle number is conserved: the dynamical state of the system oscillates between the states  $|\circ, \bullet, \circ, \dots\rangle$  and  $|\bullet, \circ, \bullet, \dots\rangle$  (where  $\circ$  corresponds to an empty dot, and  $\bullet$  to an occupied dot). This would register an imbalance which looks thermal, but a probability distribution  $p(\rho(t), n = N)$  sharply peaked around  $N = L_\rho/2$  - and thus a near-zero number entropy. We support this suggestion with a brief numerical analysis in appendix C in which we investigate the overlap of a dynamical state in a single, typical, disorder profile, with both charge-density wave states. Interestingly, we see similar behaviour in systems with an odd number of sites, suggesting a more complicated explanation which we defer to future study.

We also examine individual slices of the phase diagrams of section II in section IV, to emulate the kind of results we would expect to see from an experiment which scans  $h/\tau$  or  $V/\tau$  whilst holding the other constant. Such an experiment is far simpler (especially in the case of scanning  $h/\tau$  which can be freely tuned by modifying plunger gate voltages) than determining the full phase diagram. Panels (a) and (b) of section IV show the bulk imbalance and number entropy as we hold either  $V/\tau$  and  $h/\tau$  fixed on both sides of the MBL and metal-insulator transition and scan the other parameter respectively. Panels (c) and (d) of section IV show the local variants. The black dashed line in each panel shows the thermal value of the number entropy, a benchmark of ergodicity in the system, which we derive in appendix D.

We find that, as expected, the form of the imbalance

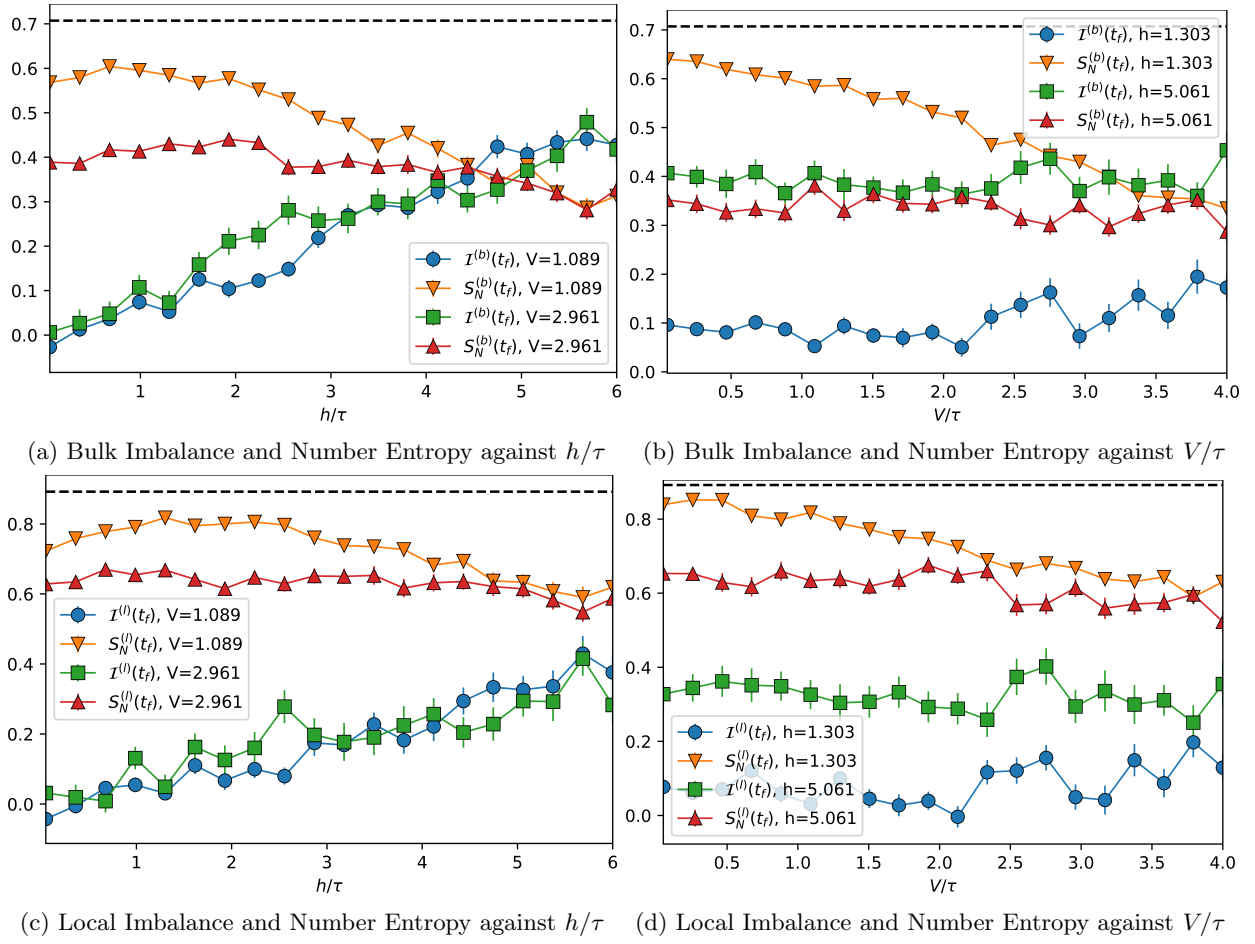


FIG. 4: Slices of the phase diagrams of section II (the realistic  $L = 8$  model) for (a) and (c) fixed values of  $V/\tau$  on both sides of the transition point between thermal and insulating phases at  $V/\tau = 2$ , and (b) and (d) fixed values of  $h/\tau$  on both sides of the crossover from thermal to MBL regimes at  $h/\tau = 3.5$ ; error bars shown where visible.

is agnostic to changes in the interaction strength  $V/\tau$ ; with each pair of imbalance curves in each panel having similar functional forms. The only difference is in panels (b) and (d) in which the imbalance is significantly higher for high  $h/\tau$  and easily differentiated from the low  $h/\tau$  case; though they are roughly invariant as we scan  $V/\tau$ .

The number entropy is clearly sensitive to both parameters, staying fixed for sufficiently high  $V/\tau$  or  $h/\tau$  as the other parameter is scanned; but showing a clear decrease with increasing  $V/\tau$  or  $h/\tau$  as the other is held at a low constant value. Panel (b) shows this difference in the behaviour of the number entropy for different values of  $V/\tau$  most clearly. The high- $h/\tau$  number entropy curve is roughly constant, whilst the low- $h/\tau$  curve shows a decrease with increasing  $V/\tau$ . Moreover, the number entropies are most readily differentiated in the thermal regime where they diverge, meeting again for sufficiently  $h/\tau$ . Importantly, this difference in behaviour becomes much harder to distinguish in (c); in which both number entropy curves are much closer together and their functional forms are harder to differentiate. This means that fixing  $V/\tau$  and extracting local imbalance and num-

ber entropy values for different  $h/\tau$  may be - by itself - insufficient to differentiate between MBL and insulating behaviour. The experimentalist may have to supplement this analysis by either considering bulk quantities instead, or by finding a way to vary  $V/\tau$  such that the imbalance and number entropy curves in panels (b) or (d) can be directly differentiated instead.

We note that our decision to restrict our analysis to a small number of disorder realizations, and our use of large absolute and relative uncertainties in all parameters, represents a worst-case scenario. Thus, experimental results are likely to be clearer than those presented in this article. Results for an ideal system are shown in appendix B, in which differentiating between the MBL and insulating regimes becomes a much easier task. Despite this, differentiation between these regimes is possible even in our conservative model. Provided that the charging energies are high enough that  $h/\tau$  can be freely tuned, local charge sensing is enough to identify MBL, and unambiguously differentiate it from insulating behaviour due to strong electron-electron interactions, in current-generation QDA.

## VI. CONCLUSIONS

Our findings show that MBL is accessible in state-of-the-art QDA, but that its identification is not a simple task. The key limitation to detecting MBL in modern quantum dot arrays is ensuring high enough on-site charging energies such that they cannot be surmounted by the large applied random chemical potentials required to localize the system. This may be improved by e.g. decreasing  $\tau$ , but that requires a corresponding increase in charge-qubit coherence times such that total evolution times are large enough to see localization. This could perhaps be achieved by designing free-standing dots that isolate the system from phonons. Working within these limitations we first characterized an experimental device and extrapolated that characterization into a worst-case model. We then numerically determined the phase diagram of the device as a function of disorder and interaction strength; identifying an insulating regime which may be mistaken for MBL. We find that the widely-used imbalance is agnostic to this phase, and propose an alternative protocol based on the number entropy - which requires the same measurements as the imbalance - and which successfully differentiates MBL from the thermal and insulating regimes. This protocol relies only on local

charge-sensing measurements, which are readily accessible in modern quantum dot experiments. In addition, we find that performing these measurements on two sites in the middle of the system yields qualitatively similar results as bulk analyses, drastically reducing the number and complexity of measurements required.

## VII. ACKNOWLEDGEMENTS

The authors acknowledge the EPSRC grant Nonergodic quantum manipulation EP/R029075/1. The authors also thank Dr. G. Stefanou for his advice and technical experimental support.

## VIII. AUTHOR CONTRIBUTIONS

A.N.-K., G.J., C.G.S., and S.B. devised the project and the main conceptual ideas. A.N.-K. developed the theoretical model and carried out the numerical simulations. G.J. designed, planned, and carried out the experiments. P.A., T.A.M., and D.A.R. contributed to the fabrication of the devices. A.N.-K. and G.J. wrote the manuscript with support and contributions from C.G.S. and S.B.

- 
- [1] R. Nandkishore and D. A. Huse, Many-body localization and thermalization in quantum statistical mechanics, *Annual Review of Condensed Matter Physics* **6**, 15 (2015).
  - [2] F. Alet and N. Laflorencie, Many-body localization: An introduction and selected topics, *Comptes Rendus Physique* **19**, 498 (2018).
  - [3] D. A. Abanin and Z. Papić, Recent progress in many-body localization, *Ann. Phys. (Leipzig)* **529**, 1700169 (2017).
  - [4] D. A. Abanin, E. Altman, I. Bloch, and M. Serbyn, Colloquium: Many-body localization, thermalization, and entanglement, *Rev. Mod. Phys.* **91**, 021001 (2019).
  - [5] M. Schreiber, S. S. Hodgman, P. Bordia, H. P. Lüschen, M. H. Fischer, R. Vosk, E. Altman, U. Schneider, and I. Bloch, Observation of many-body localization of interacting fermions in a quasirandom optical lattice, *Science* **349**, 842 (2015).
  - [6] H. P. Lüschen, P. Bordia, S. S. Hodgman, M. Schreiber, S. Sarkar, A. J. Daley, M. H. Fischer, E. Altman, I. Bloch, and U. Schneider, Signatures of many-body localization in a controlled open quantum system, *Phys. Rev. X* **7**, 011034 (2017).
  - [7] J.-y. Choi, S. Hild, J. Zeiher, P. Schauß, A. Rubio-Abadal, T. Yefsah, V. Khemani, D. A. Huse, I. Bloch, and C. Gross, Exploring the many-body localization transition in two dimensions, *Science* **352**, 1547 (2016).
  - [8] J. Smith, A. Lee, P. Richerme, B. Neyenhuis, P. W. Hess, P. Hauke, M. Heyl, D. A. Huse, and C. Monroe, Many-body localization in a quantum simulator with programmable random disorder, *Nature Physics* **12**, 907 (2016).
  - [9] P. Roushan, C. Neill, J. Tangpanitanon, V. M. Bastidas, A. Megrant, R. Barends, Y. Chen, Z. Chen, B. Chiaro, A. Dunsworth, A. Fowler, B. Foxen, M. Giustina, E. Jeffrey, J. Kelly, E. Lucero, J. Mutus, M. Neeley, C. Quintana, D. Sank, A. Vainsencher, J. Wenner, T. White, H. Neven, D. G. Angelakis, and J. Martinis, Spectroscopic signatures of localization with interacting photons in superconducting qubits, *Science* **358**, 1175 (2017).
  - [10] C. Berke, E. Varvelis, S. Trebst, A. Altland, and D. P. DiVincenzo, Transmon platform for quantum computing challenged by chaotic fluctuations, *Nature Communications* **13**, 10.1038/s41467-022-29940-y (2022).
  - [11] T. Hensgens, T. Fujita, L. Janssen, X. Li, C. J. V. Diepen, C. Reichl, W. Wegscheider, S. D. Sarma, and L. M. K. Vandersypen, Quantum simulation of a fermi-hubbard model using a semiconductor quantum dot array, *Nature* **548**, 70 (2017).
  - [12] U. Mukhopadhyay, J. P. Dehollain, C. Reichl, W. Wegscheider, and L. M. Vandersypen, A  $2 \times 2$  quantum dot array with controllable inter-dot tunnel couplings, *Applied Physics Letters* **112**, 183505 (2018).
  - [13] W. G. van der Wiel, S. D. Franceschi, J. M. Elzerman, T. Fujisawa, S. Tarucha, and L. P. Kouwenhoven, Electron transport through double quantum dots, *Reviews of Modern Physics* **75**, 1 (2002).
  - [14] R. K. Panda, A. Scardicchio, M. Schulz, S. R. Taylor, and M. Žnidarič, Can we study the many-body localisation transition?, *Europhysics Letters* **128**, 67003 (2020).
  - [15] P. Sierant and J. Zakrzewski, Challenges to observation of many-body localization, *Phys. Rev. B* **105**, 224203 (2022).



- [16] V. Khemani, D. N. Sheng, and D. A. Huse, Two universality classes for the many-body localization transition, *Phys. Rev. Lett.* **119**, 075702 (2017).
- [17] F. R. Braakman, P. Barthelémy, C. Reichl, W. Wegscheider, and L. M. K. Vandersypen, Long-distance coherent coupling in a quantum dot array, *Nature Nanotechnology* **8**, 432 (2013).
- [18] M. Field, C. G. Smith, M. Pepper, D. A. Ritchie, J. E. F. Frost, G. A. C. Jones, and D. G. Hasko, Measurements of coulomb blockade with a noninvasive voltage probe, *Phys. Rev. Lett.* **70**, 1311 (1993).
- [19] C. Volk, A. M. J. Zwerver, U. Mukhopadhyay, P. T. Een-debak, C. J. van Diepen, J. P. Dehollain, T. Hensgens, T. Fujita, C. Reichl, W. Wegscheider, and L. M. K. Vandersypen, Loading a quantum-dot based “qubyte” register, *npj Quantum Information* **5** (2019).
- [20] T. Hayashi, T. Fujisawa, H. D. Cheong, Y. H. Jeong, and Y. Hirayama, Coherent manipulation of electronic states in a double quantum dot, *Phys. Rev. Lett.* **91**, 226804 (2003).
- [21] K. D. Petersson, J. R. Petta, H. Lu, and A. C. Gossard, Quantum coherence in a one-electron semiconductor charge qubit, *Phys. Rev. Lett.* **105**, 246804 (2010).
- [22] J. Gorman, D. G. Hasko, and D. A. Williams, Charge-qubit operation of an isolated double quantum dot, *Phys. Rev. Lett.* **95**, 090502 (2005).
- [23] J. R. Petta, A. C. Johnson, J. M. Taylor, E. A. Laird, A. Yacoby, M. D. Lukin, C. M. Marcus, M. P. Hanson, and A. C. Gossard, Coherent manipulation of coupled electron spins in semiconductor quantum dots, *Science* **309**, 2180 (2005), <https://www.science.org/doi/pdf/10.1126/science.1116955>.
- [24] H. Bluhm, S. Foletti, I. Neder, M. Rudner, D. Mahalu, V. Umansky, and A. Yacoby, Dephasing time of gaas electron-spin qubits coupled to a nuclear bath exceeding 200  $\mu$ s, *Nature Physics* **7**, 109 (2011).
- [25] E. Kawakami, T. Jullien, P. Scarlino, D. R. Ward, D. E. Savage, M. G. Lagally, V. V. Dobrovitski, M. Friesen, S. N. Coppersmith, M. A. Eriksson, and L. M. K. Vandersypen, Gate fidelity and coherence of an electron spin in an si/SiGe quantum dot with micromagnet, *Proceedings of the National Academy of Sciences* **113**, 11738 (2016).
- [26] T. Hensgens, *Emulating Fermi-Hubbard physics with quantum dots: from few to more and how to*, Ph.D. thesis, Delft University of Technology (2018), casimir PhD series 2017-47.
- [27] X. Wang, S. Yang, and S. Das Sarma, Quantum theory of the charge-stability diagram of semiconductor double-quantum-dot systems, *Phys. Rev. B* **84**, 115301 (2011).
- [28] Z. Shi, C. B. Simmons, D. R. Ward, J. R. Prance, R. T. Mohr, T. S. Koh, J. K. Gamble, X. Wu, D. E. Savage, M. G. Lagally, M. Friesen, S. N. Coppersmith, and M. A. Eriksson, Coherent quantum oscillations and echo measurements of a si charge qubit, *Phys. Rev. B* **88**, 075416 (2013).
- [29] B.-C. Wang, B.-B. Chen, G. Cao, H.-O. Li, M. Xiao, and G.-P. Guo, Coherent control and charge echo in a gaas charge qubit, *Europhysics Letters* **117**, 57006 (2017).
- [30] Moreover,  $\tau$  can be directly controlled by tuning the voltages applied to the barrier gates which separate dots, as evidenced by the ability to ‘pinch off’ a dot (isolate it) before e.g. a measurement. This makes  $\tau$  the parameter which is easiest to control *in situ* - without having to fabricate a new device.
- [31] J. H. Bardarson, F. Pollmann, and J. E. Moore, Unbounded growth of entanglement in models of many-body localization, *Phys. Rev. Lett.* **109**, 017202 (2012).
- [32] M. Serbyn, Z. Papić, and D. A. Abanin, Universal slow growth of entanglement in interacting strongly disordered systems, *Phys. Rev. Lett.* **110**, 260601 (2013).
- [33] K. Xu, J.-J. Chen, Y. Zeng, Y.-R. Zhang, C. Song, W. Liu, Q. Guo, P. Zhang, D. Xu, H. Deng, *et al.*, Emulating many-body localization with a superconducting quantum processor, *Physical review letters* **120**, 050507 (2018).
- [34] A. Lukin, M. Rispoli, R. Schittko, M. E. Tai, A. M. Kaufman, S. Choi, V. Khemani, J. Léonard, and M. Greiner, Probing entanglement in a many-body-localized system, *Science* **364**, 256 (2019).
- [35] R. Yousefjani, S. Bose, and A. Bayat, Non-algebraic entanglement growth in long-range many-body localized systems, *arXiv preprint arXiv:2201.03716* (2022).
- [36] D. J. Luitz, N. Laflorencie, and F. Alet, Extended slow dynamical regime close to the many-body localization transition, *Phys. Rev. B* **93**, 060201 (2016).
- [37] P. Bordia, H. Lüschen, U. Schneider, M. Knap, and I. Bloch, Periodically driving a many-body localized quantum system, *Nature Physics* **13**, 460 (2017).
- [38] H. P. Lüschen, P. Bordia, S. Scherg, F. Alet, E. Altman, U. Schneider, and I. Bloch, Observation of slow dynamics near the many-body localization transition in one-dimensional quasiperiodic systems, *Phys. Rev. Lett.* **119**, 260401 (2017).
- [39] A. Nico-Katz, A. Bayat, and S. Bose, Memory hierarchy for many-body localization: Emulating the thermodynamic limit, *Phys. Rev. Research* **4**, 033070 (2022).
- [40] M. Kiefer-Emmanouilidis, R. Unanyan, M. Fleischhauer, and J. Sirker, Evidence for unbounded growth of the number entropy in many-body localized phases, *Physical Review Letters* **124**, 10.1103/physrevlett.124.243601 (2020).
- [41] R. Ghosh and M. Žnidarič, Resonance-induced growth of number entropy in strongly disordered systems, *Phys. Rev. B* **105**, 144203 (2022).
- [42] C.-J. Lin and O. I. Motrunich, Exact quantum many-body scar states in the rydberg-blockaded atom chain, *Physical review letters* **122**, 173401 (2019).
- [43] H. Bernien, S. Schwartz, A. Keesling, H. Levine, A. Omran, H. Pichler, S. Choi, A. S. Zibrov, M. Endres, M. Greiner, V. Vuletić, and M. D. Lukin, Probing many-body dynamics on a 51-atom quantum simulator, *Nature* **551**, 579 (2017).
- [44] V. Khemani, C. R. Laumann, and A. Chandran, Signatures of integrability in the dynamics of rydberg-blockaded chains, *Physical Review B* **99**, 161101 (2019).
- [45] L. D’Alessio, Y. Kafri, A. Polkovnikov, and M. Rigol, From quantum chaos and eigenstate thermalization to statistical mechanics and thermodynamics, *Advances in Physics* **65**, 239 (2016), <https://doi.org/10.1080/00018732.2016.1198134>.
- [46] D. N. Page, Average entropy of a subsystem, *Physical Review Letters* **71**, 1291 (1993).

## Appendix A: Mapping the Fermi-Hubbard Model to the XXZ Spin Chain

The spinless Fermi-Hubbard model of eq. (1) can be mapped onto a spin-1/2 XXZ model by means of a standard Jordan-Wigner transformation. We start by identifying the two states of each site - occupied or unoccupied - with the two spin-1/2 states - spin-up and spin-down. We then relate the fermionic creation and annihilation operators with the spin-1/2 raising and lowering operators  $c_j^\dagger \rightarrow S_j^+$  and  $c_j \rightarrow S_j^-$ , and impose the standard fermionic anti-commutators by applying highly non-local Jordan-Wigner string operators such that the final transformation takes the form:

$$c_j^\dagger = \left( \prod_{k < j} \sigma_k^z \right) S_j^+ \quad (\text{A1})$$

$$c_j = \left( \prod_{k < j} \sigma_k^z \right) S_j^- \quad (\text{A2})$$

where the  $\sigma_j^z$  is the standard Pauli Z operator. In practice, due to the fact that  $(\sigma_j^z)^2 = 1$ , many of these Jordan-Wigner strings cancel and one can often manipulate the final Hamiltonian into a local form. Substituting eq. (A1) and eq. (A2) into the Hamiltonian eq. (1), and simplifying the Jordan-Wigner strings, yields the model

$$H = \tau \sum_j^{L-1} (S_j^+ \sigma_j^z S_{j+1}^- + \text{h.c.}) \\ + V \sum_j^{L-1} S_j^+ S_j^- S_{j+1}^+ S_{j+1}^- + \sum_j^L h_j S_j^+ S_j^-$$

which we can simplify further by noting that  $S_j^+ S_j^- = S_j^z + 1/2$ , that  $S_j^+ \sigma_j^z = -S_j^+$ , and by invoking the definition of  $S_j^\pm = S_j^x \pm i S_j^y$ ; where  $S_j^\alpha$  are the standard spin-1/2 operators. Under these simplifications, the model now takes the form

$$H = -2\tau \sum_j^{L-1} (S_j^x S_{j+1}^x + S_j^y S_{j+1}^y) \\ + V \sum_j^{L-1} (S_j^z S_{j+1}^z + S_j^z + S_{j+1}^z + 1) \\ + \sum_j^L h_j (S_j^z + 1/2)$$

wherein the negative overall phase of the tunnelling term proportional to  $t$  is irrelevant to the physics of the system: we can e.g. simply relabel every other site such that, for odd  $j$ ,  $S_j^{x/y} \rightarrow -S_j^{x/y}$ , and  $S_j^z$  is left unchanged. We eliminate all constant terms which do not contribute to the physics of the system, and note that - since the

Hamiltonian conserved total particle number, its Jordan-Wignerization equivalently conserves total spin. Thus we can neglect all terms proportional to  $\sum_j^L S_j^z$ , which appear in the sum over single-site operators proportional to  $V$  such that  $\sum_j^{L-1} S_j^z + S_{j+1}^z = -S_1^z - S_L^z + \sum_j^L S_j^z$ . Collecting terms, and performing these substitutions gives us an extended XXZ Hamiltonian

$$H = 2\tau \sum_j^{L-1} \left( S_j^x S_{j+1}^x + S_j^y S_{j+1}^y + \frac{V}{2t} S_j^z S_{j+1}^z \right) \\ - V (S_1^z + S_L^z) + \sum_j^L h_j S_j^z$$

which exhibits an XXZ transition at  $V = 2\tau$ , makes clear the importance of edge effects in small systems by explicit inclusion of the dangling  $S_1^z$  and  $S_L^z$  operators.

## Appendix B: Ideal phase diagrams for a system of size $L=10$

In section V of the main text, we analyzed the von Neumann entropy, the imbalance, and the number entropy in both bulk and local variants (see section IV of the main text for definitions and discussion) respectively. There we considered a highly conservative realistic scenario: with constraints placed on evolution times, number of disorder realizations, and parameter characterization errors. Here we present similar results but for an 'ideal' system of  $L = 10$  sites, exponential time scales of  $\tau t_f = 10^{10}$ , late-time time-averaging - wherein we average over the final third of the evolution time to eliminate remaining fluctuations - and 512 disorder realizations. Additionally, we eliminate the absolute and relative uncertainties in the parameters  $h/\tau$  and  $V/\tau$  in the main text.

The results of this analysis of an ideal system are shown in appendix A, and are qualitatively similar to the corresponding results in the main text: the imbalance is agnostic to changes in  $V/\tau$  and cannot detect the insulating regime at  $V/\tau > 2$ , this is in contrast to the von Neumann and number entropies which identify both this transition and the ergodic-MBL crossover at  $h/\tau \sim 3.5$ . Strikingly, the local variants which use measurements on only two sites in the middle of the array are qualitatively similar to the bulk variants, indicating that local measurements are enough to identify the different regimes.

Individual slices of the phase diagrams of the ideal system shown in appendix A are shown in appendix B, wherein we fix  $V/\tau$  or  $h/\tau$  and scan the other respectively. The behaviours noted in section V of the main text are much clearer in the larger, ideal system. The imbalance is clearly agnostic to changes in  $V/\tau$ , as evidenced by its constancy in panels (b) and (d) of appendix B. Moreover, the imbalance curves in panels (a) and (c) respectively are almost identical. This supports the protocol we propose which requires different post-processing on charge measurements to construct both the

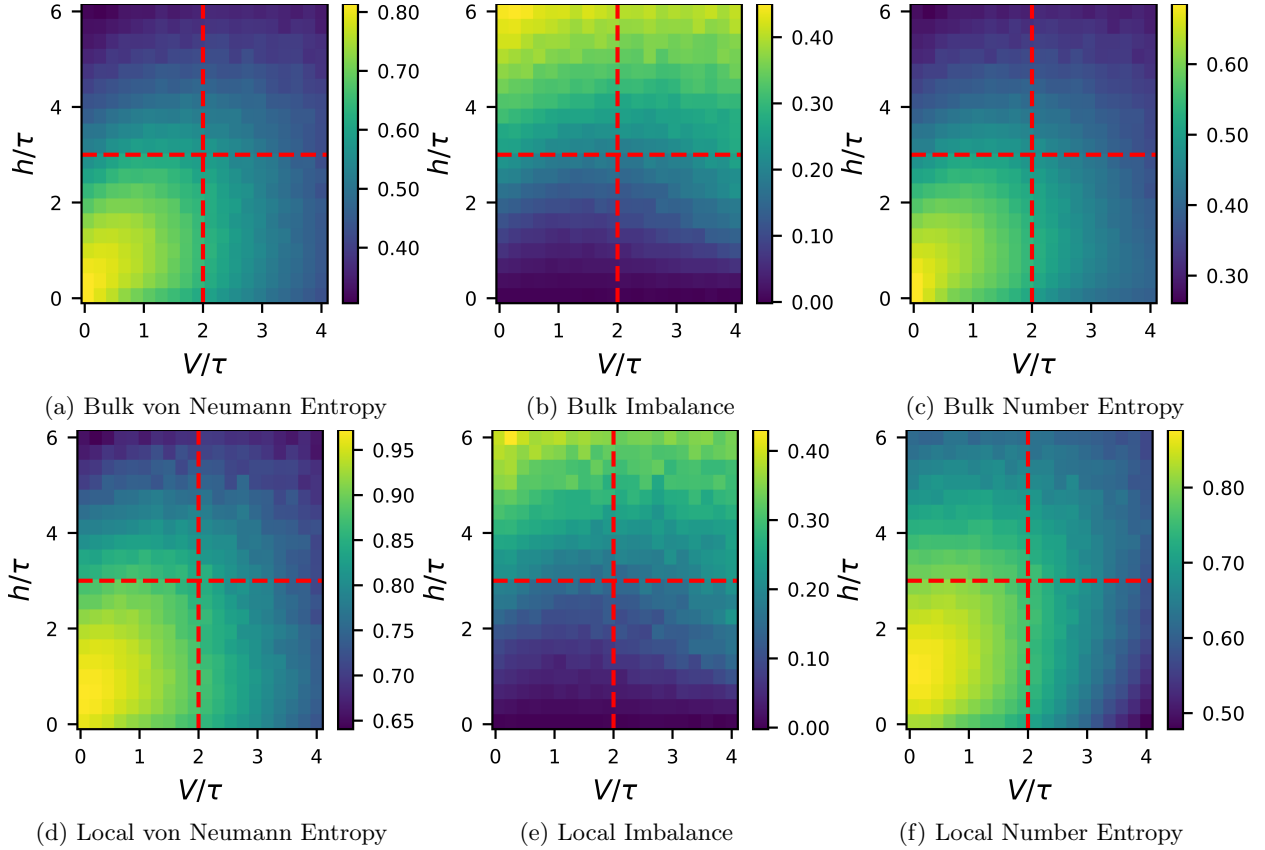


FIG. 5: Time and disorder-averaged steady-state quantities across the full  $V - h$  phase diagram for the ideal system; initialized in a charge-density wave configuration. The ideal system consists of  $L = 10$  sites, exponential total evolution times of  $\tau t_f = 10^{10}$ , time-averaging over the final third of the total evolution time, and disorder-averaging over 512 samples per  $(V, h)$  coordinate.

imbalance and number entropy in tandem. The number entropy has clearly different behaviour as both  $V/\tau$  and  $h/\tau$  vary, staying fixed for sufficiently high  $V/\tau$  or  $h/\tau$ . Panel (b) shows this behaviour most clearly, with both the imbalance and number entropy constant with increasing  $V/\tau$  for high disorder, and with imbalance constant but number entropy decreasing with increasing  $V/\tau$  for low disorder.

### Appendix C: Oscillating Insulating State

In the main text we note that a potential explanation for observing thermal values for the imbalance, but low number entropies, is by a ‘rolling’ behaviour in which the state of the system moves coherently from left to right. Here we provide some preliminary evidence for this explanation.

We initialize a system in the charge-density wave  $|\psi(0)\rangle = |\bullet, \circ, \bullet, \dots\rangle$  (where  $\circ$  corresponds to an empty dot, and  $\bullet$  to an occupied dot) and select a typical disorder profile of strength  $h/\tau = 1$ . In fig. 7 we then investigate the overlap of the state  $|\psi(t)\rangle$  with  $|\psi(0)\rangle$

in panel (a) and its overlap with the complementary charge-density wave state  $|\circ, \bullet, \circ, \dots\rangle$  in panel (b). We compute the overlap as the expectation value *squared*:  $|\langle\psi(t)|\psi_{\text{target}}\rangle|^2$ . For low  $V/\tau$  (thermal regime), we see both curves drop rapidly to low values and remain there. But as we increase  $V/\tau$  we see sharp revivals in the overlap of  $|\psi(t)\rangle$  with both charge-density wave states. The first peak in panel (a) (after  $t = 0$ ) occurs after the first peak in panel (b) and at approximately the same time difference as the first peak in panel (b) does from  $t = 0$ . This suggests that our ‘rolling’ behaviour explanation may be a good approximation to the dynamics of the state; though a more detailed investigation is warranted. Such an investigation is beyond the scope of this article.

### Appendix D: Derivation of the Infinite-Temperature Thermal Number Entropy

We start by assuming that, given  $L$  sites populated by  $N_0$  electrons, computational microstates which conserve  $N_0$  are equally probable i.e. that the microcanonical ensemble gives the correct physical description of the

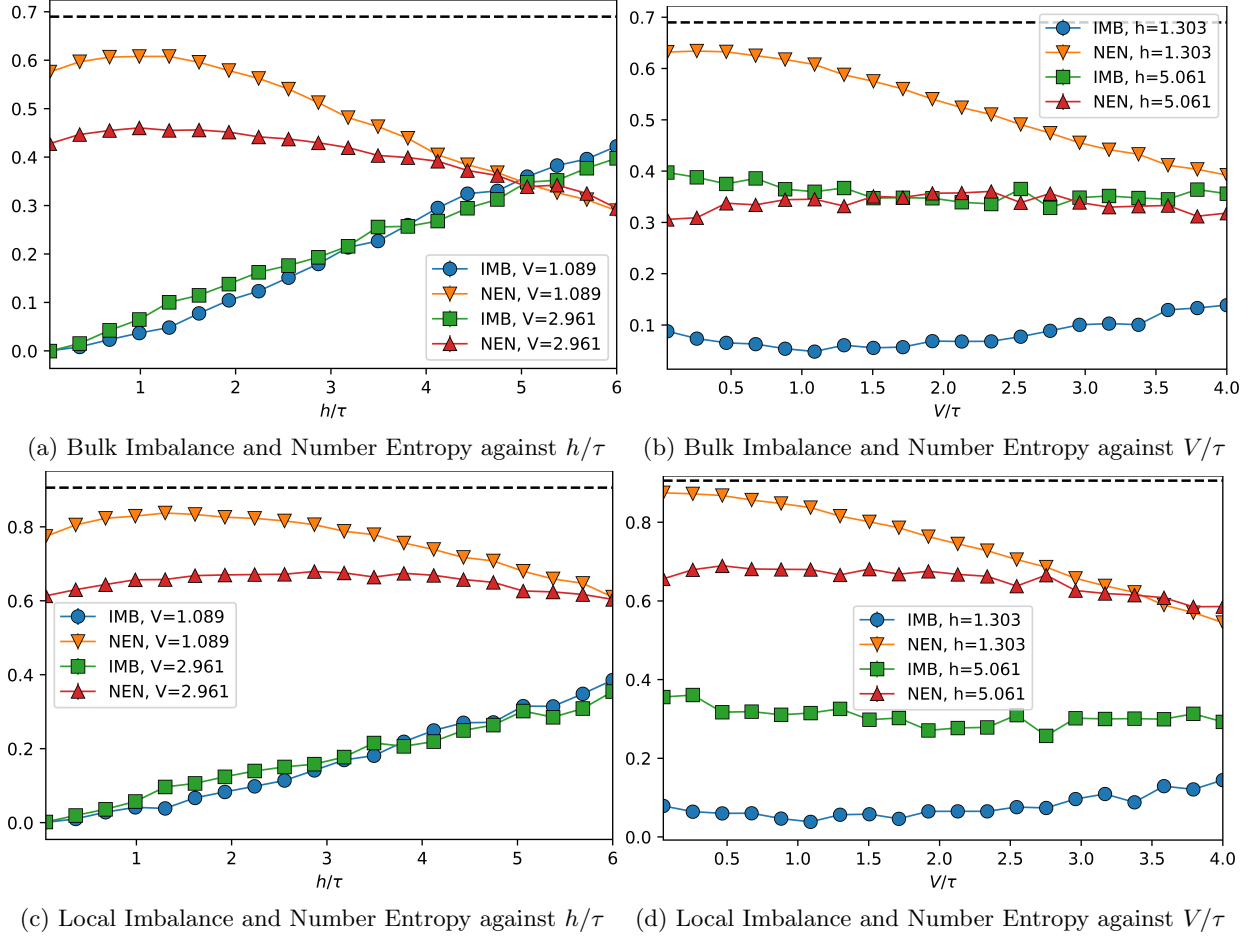


FIG. 6: Slices of the phase diagrams of appendix A (the ideal  $L = 10$  model) for (a) and (c) fixed values of  $V/\tau$  on both sides of the transition point between thermal and insulating phases at  $V/\tau = 2$ , and (b) and (d) fixed values of  $h/\tau$  on both sides of the crossover from thermal to MBL regimes at  $h/\tau = 3.5$ ; error bars shown where visible.

equilibrated system at late time [45]. The problem of deriving the probability distribution  $p_k(n)$  of observing  $n$  electrons within  $k$  selected sites becomes straightforward. The probability  $p_k(n = N)$  is simply the probability of detecting  $N$  occupied sites and  $k - N$  empty sites, multiplied by the multiplicity  $\binom{k}{N}$  of such microstates:

$$p_k(n = N) = \binom{k}{N} \underbrace{\left[ \prod_{j=0}^{N-1} \frac{n_0 - j}{L - j} \right]}_{\text{occupied}} \underbrace{\left[ \prod_{j=0}^{k-N-1} 1 - \frac{n_0 - N - j}{L - N - j} \right]}_{\text{empty}} \quad (\text{D1})$$

The number entropy  $S_N$  of such an infinite-temperature subsystem is then readily calculated according to eq. (4) of the main text with  $\rho(t) \rightarrow \rho_{\text{th}}$ . This quantity serves - in a similar capacity as the page entropy - as a thermal limiting case for the number entropy [46].

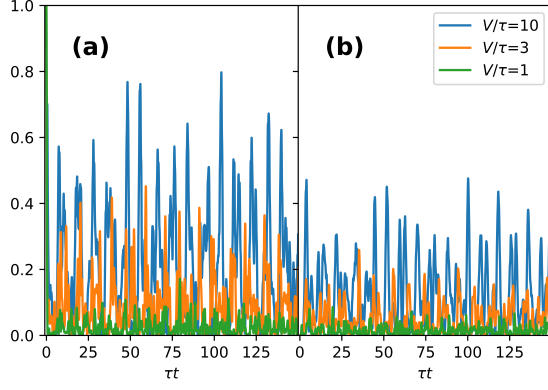


FIG. 7: Numerical evidence of coherent oscillation of a charge-density wave between two configurations as  $V/\tau$ .

For a system initialized in the state  $|\bullet, \circ, \bullet, \dots\rangle$  (a) shows overlap with the initial state and (b) shows the overlap with the inverted state  $|\circ, \bullet, \circ, \dots\rangle$ . System hamiltonian is a typical disorder-realization of strength  $h/\tau = 1$ .